Article

Methodology and Guidelines for Designing Flexible BMS in Automotive Applications

Napat Trongnukul[1,a], Nisai H. Fuengwarodsakul[1,b,*], and Manop Masomtob[2,c]

1 The Sirindhorn International Thai-German Graduate School of Engineering, King Mongkut's University of Technology North Bangkok, 1518 Pracharat 1 Road Bangsue Bangkok 10800 Thailand
2 National Energy Technology Center (ENTEC), National Science and Technology Development Agency (NSTDA), 111 Thailand Science Park, Phahonyothin Road, Khlong Nueng, Khlong Luang, Pathum Thani, 12120, Thailand
E-mail: [a]joe_napat@hotmail.com, [b,*]nisai.f@tggs.kmutnb.ac.th (Corresponding author), [c]manop.mas@entec.or.th

Abstract. The fragile characteristics of Li-ion batteries lead to the need of battery management system (BMS) to carefully supervise them during the operation. Since there are so many variations in battery configurations, the BMS usually must undergo many iterations of the development cycle, which take a long time to optimize and finalize the design. Previously, many works adopted the idea of modularized BMS to address these issues, but they still have some skeptical issues such as measurement approaches or difficulties in reconfiguration. This paper presents a guideline on the crucial aspects of flexible BMS designs for automotive applications, which aims to reduce time and effort for developing a new BMS for automotive battery pack. The guideline covers some crucial aspects pertaining the automotive BMS hardware implementation, SOC estimation algorithm and its computational performance based on Extended Kalman Filter (EKF) and Luenberger Observer (LO) with 3 levels of Electrochemical model (ECM). All of the tests were carried out in a small-scale microcontroller. It was found that 2-RC ECM gives the best trade-off between SOC estimation accuracy and computational time. While the 3-RC ECM provides 9.5% and 31% higher accuracy than the 2-RC and 1-RC ECM, respectively, but taking 88% and 240% higher computational time than the latter two cases. The optimal speed of the observer poles of LO algorithm are suggested to be in the range of 2-5 times faster than the system poles, which makes the convergence speed to be comparable to the EKF algorithm but is still able to keep the SOC estimation error in the range of 3-5%. These results can be used to make a trade-off between estimation accuracy and computational time, to select the optimal SOC estimation algorithm for onboard BMSs.

Keywords: Flexible battery management, SOC estimation, battery modelling, equivalent circuit modelling.

1. Introduction

Lithium-ion (Li-ion) batteries are a promising battery technology used across various applications in modern days, due to their high energy density and lightweight characteristic. However, Li-ion batteries are naturally prone to overcharge/over-discharge, which might lead to irreversible damage to the cell chemistry [1]. Therefore, Li-ion batteries require a battery management system (BMS) to enhance the reliability/performance of the battery pack. Each battery application has different variations, such as cell configuration, cell chemistry, etc. Especially for automotive industries where these variations are complicated. So, the BMS needs to be adjusted along with these variations to work properly and achieve its highest performance. This adjustment usually takes a long time and a lot of resources to finish. Therefore, it would be very beneficial to develop a flexible BMS to shorten the development cycle, time, and resources required to reconfigure the system.

Flexible BMS, in its sense, is a platform in which the number of monitoring units can be freely adjusted to support a wide range of battery cells, voltage, chemistries, and balancing algorithms, etc. In the past, there were several studies that worked on the design of flexible BMS [1-3, 5-7, 9-10, 12], the common things found in these studies is that they used a decentralized structure to maximize scalability and flexibility [16]. However, each study focuses on different aspects according to the main purpose of the design. The flexible BMS in [2, 7] aims to develop low-cost stackable BMS, the system is composed of multiple local units and a master unit, connected together via LIN Bus/ highspeed UART. The SOC estimation and balancing strategy are very simple, resulting in a low computational burden. In [3], the author minimizes the overall cost by using low-cost STM32 and Scilab/Xcos to implement model-in-the-loop (MiL) to simulate real-time battery modelling, resulting in better SOC estimation. In [10, 12], the authors focus on the implementation of external communication between master unit and outside systems, such as SPI, RS485, Ethernet, CAN or internet of thing (IoT), which supports the exchange of battery information in both stationary and automotive applications. Even though these studies focus on different purposes, the key points in developing a flexible BMS are typically lying in six crucial aspects 1) voltage measurement and sampling time 2) current measurement 3) Interconnection between BMS modules 4) Balancing Algorithm 5) Temperature measurement 6) SOC estimation algorithm, as shown in Fig. 1. The in-depth detail of how to properly design the hardware/ software for a particular BMS application regarding these aspects is rarely mentioned in any previous works, as shown in the following literature review.
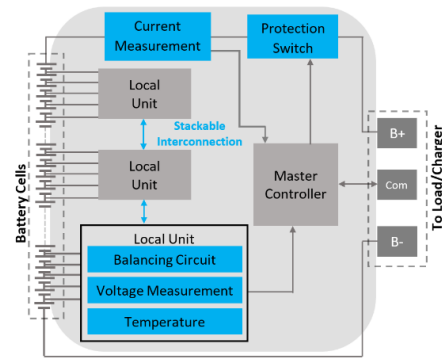

Fig. 1. Essential components of flexible BMS.

1. Current sensor in flexible BMS shall be chosen based on the range of load current, noise sensitivity, thermal drift, and common mode voltage [13]. In [8, 9] modular BMS for low-voltage batteries was designed using a high-side shunt-based current sensor, but it has an issue with input common-mode voltage [11, 14]. In [1, 3], the low-side hall sensor is used as the current sensor. Even though it has no problem with input common mode voltage, but the accuracy, thermal drift, and noise sensitivity might be inferior to the shunt-based sensor [13], which might be a serious issue when the BMS is being used in unusual high/low temperatures or in a noisy environment.

2. Voltage measurement in [5], the author designed the modular BMS by using an instant IC to monitor 7.2V NiMH battery cells by using the combination between the resistor divider and the differential amplifier. This method is good for modularity since it reduces the cell voltage by half, resulting in a smaller number of required BMS ICs. However, this method might cause an unacceptable measurement error due to the tolerance of resistors. In [1, 6], the cell voltage measurement is achieved by using non-isolated amplifiers attached to every single cell. This method requires a ground separation between local units and microcontroller for safety issue [4]. Moreover, installing these amplifiers requires a huge soldering work, making it not practical for a modular design in which the number of cells or the measurement range can be arbitrarily changed.

3. Balancing algorithm in [10] uses voltage-based algorithm to start the balancing process when the cell voltage exceeds or drops beyond a particular threshold. This algorithm is easy to implement, but the terminal voltage might not reflect the actual SOC due to the ohmic voltage drop. In [7], the author uses the SOC value obtained from the coulomb-counting method to perform balancing. This method is more accurate than the voltage-based since the SOC is not disturbed by the ohmic voltage drop. However, the Coulomb-counting method does not have a self-correction mechanism, so its accuracy might deteriorate over time due to the accumulated measurement errors [15]. In [3], the balancing is implemented based on electrochemical impedance

spectroscopy (EIS) model with an Extended Kalman Filter (EKF). This method can accurately perform real-time balancing, but the EIS method has very limited flexibility since it requires the use of a specialized load profile, making it suitable for parameter initialization only [15] but not a good for a flexible BMS in which the type of cell/ cell chemistries is uncertain. In [2, 7] a modular BMS aims to shorten the balancing time by using external FETs to provide high balancing current. But the system requires a large heatsink to deal with high power dissipation, making the BMS module bulky and not suitable for flexible design. In reality, the balancing current found in medium-size EVs is not too high [16].

4. Intercommunication between each BMS is a key factor that allows BMS to become stackable. In [5, 7], use 4-wires non-isolated SPI as a main communication between each local units, so it is necessary to keep the wiring short to minimize delays and noise [17]. This issue makes the non-isolated SPI not suitable for flexible BMS in which each BMS module might be far away from the other [20].

It can be seen that there are still some issues regarding the design of flexible BMS that need to be clarified, so this study aims to provide a guideline on the design of flexible BMS hardware for automotive applications, covering the six important aspects mentioned previously, to reduce the time which a BMS designer has to spend on doing research or carry out comparisons. Apart from all of the issues mentioned above, other equally important points in flexible BMS implementation are the ability to estimate battery internal resistance and SOC value in real-time. The internal resistance can be used to reflect the state of health (SOH) of the battery, whereas the accurate SOC value can enhance the balancing performance, leading to longer battery life. However, these real-time estimations shall not consume too long computational time, as it will reduce the number of cells which a flexible BMS can support. The scope of battery cells in consideration of this study is lying on only Li-ions battery packs for small to medium scale vehicles, whose number of cells is up to 100 cells, the maximum capacity is up to 100 kWh, cell capacity up to 100 Ah. The pack voltage is in the range of 36-400 V, and the voltage measurement is in the range of 0-5 V to support all types of battery chemistries, including super capacitors.

The structure of this study is organized as follows: Section 2 introduces some details and recommendations associated with the six crucial aspects of the hardware design of flexible BMS, by considering the real-world operating conditions of EVs and Automotive Safety Integrity Level (ASIL). Section 3 includes the analysis and comparison of SOC estimation algorithms based on the Extended Kalman filter (EKF) and Luenberger observer (LO) under 3 levels of ECM, by using an open-source standard driving cycle battery dataset [53]. Also, Sect. 3.4 and Sect. 3.5 investigate the dynamic performance and computation time of each algorithm, to find out the

optimal balance between estimation accuracy and computational burden.

2. Battery Management Hardware Recommendation in Automotive Applications

2.1. Current Measurement for Battery Management

In automotive BMSs, there are two methods widely used to measure current, shunt-based and hall-based. Shunt-based sensors is popular due to low parasitic inductance, low-temperature drift, and high accuracy. The two most common types of shunt resistors are surface-mounted-device shunt resistors (SMD) and Kelvin connection resistors. SMD resistors have high accuracy, low thermal drift and small package, but usually suffers from contact resistance [28]. Thus, in high-current applications, Kelvin connection resistors are more preferable since the high-current path is separated from the voltage measuring points [28], resulting in low contact resistance. Kelvin connection resistors are highly recommended if the shunt resistance is lower than 500 μΩ [14]. Hall-based sensors are another popular option since they naturally provide isolation and have very low power dissipation, making them suitable for applications where the load current is above 200 A [59]. However, Hall-based sensors are practically less accurate, noisier, more susceptible to the external magnetic field and temperature change [13].

In terms of placement, there are two arrangements for placing a current sensor, low-side and high-side configuration. In the high-side configuration, the shunt resistor is placed between the battery positive pole and the load so it does not create ground disturbances, while the low-side shunt allows all load current to flow along the ground path, creating ground noise which might be problematic for the communication between load side and controller side [18]. The high-side shunt can detect a ground fault condition, whereas the low-side shunt is bypassed from the short-circuit path [18]. The amplifier used with a high-side shunt must be able to withstand high common-mode voltage [29] and load dump conditions, which generates an extra across the shunt resistor when the load is abruptly disconnected [19, 20]. Also, if the battery pack voltage exceeds 48 V, a galvanic isolation is required [14]. When using a low-side shunt, the common mode voltage is much lower, so non-isolated amplifier with a common-mode voltage of less than 36V can be used, which is easy to find and not as costly as the isolated type. The comparison of each current measurement method is shown in Table 1.

For PHEVs, EVs, HEVs, the battery current is in the range of mA to kA [21, 22], or 1:1000000 measurement ratio. The accuracy of current measurement must be maintained at 0.5-1% for current up to 450A to meet ASIL-C requirements [23]. In addition, the operating temperature of the current sensor must cover the range of

-40 to 125 ºC. To meet these requirements, the hall-based sensor becomes more expensive and bulkier than the shunt type at the same power rating. Instead, Kelvin connection resistors in the range of 50µΩ to 500µΩ complemented with an isolated modulator is more preferable due to their high resolution (>14 bits) and low power dissipation. However, the span of 1:100000 measurement ratio is not practical since it requires at least 17 bits resolution to cover this span [24]. This high-resolution measurement is very sensitive to noise and requires complicated circuit design [25]. Thus, the range of current measurement should be divided into at least 2 sub-ranges, covering the span of 1:1000, so the resolution of ADC can be in the range of 11 to 14 bits. At this resolution, ΔΣ ADC is recommended to provides low quantization noise, resulting in higher accuracy [14]. For small electric vehicles such as scooters, electric bikes or golf cart, the voltage range of a battery pack is usually in the range of 48V to 54V with continuous discharging current in the range of 10-100 A [26, 27], which is considered as low-voltage subsystem. So, the isolation barrier is typically not required. In this case, the low-side SMD resistors complemented with a non-isolated amplifier is the most cost-effective solution in term of accuracy, thermal drift, measurement range and ground fault detection.

Table 1. Comparison of widely used current sensing approaches in battery management.

Solution	Accuracy [15]	Thermal Drift [13]	Current Range [28]	Common Mode Voltage [13, 24]	Bandwidth [22]	Noise Sensitivity [13, 22]	Sample Resolution [22]	Power Loss (W)
Shunt + non-isolated amplifier	0.5% - 1%	Moderate	50-1400 A	-4 to 80 V	Up to 300 kHz	Low	n/a	2-50
Kelvin Shunt + isolated amplifier	0.1%-1%	High	120-1400 A	up to 275 V	Up to 300 kHz	Very Low	11 bits	7 – 50
Shunt + isolated modulator	0.5% - 1%	Very High	50-1400 A	up to 275 V	> 1 MHz	Very Low	>14 bits	2-50
Kelvin Shunt + isolated modulator	0.1%-1%	Very High	120-1400 A	up to 275 V	> 1 MHz	Very Low	>14 bits	7 – 50
Shunt + isolated amplifier	0.5% - 1%	High	50-1400 A	up to 275 V	Up to 300 kHz	Very Low	11 bits	2-50
Kelvin Shunt + non-isolated amplifier	0.1%-1%	High	120-1400 A	-4 to 80 V	Up to 300 kHz	Low	n/a	7 – 50
Hall Sensors	Less than 2% (Needs Calibration)	Moderate	50-2000A	Not required	100-300 kHz	High	n/a	Approximately 10

2.2. Voltage Measurement for Battery Management

There are two aspects regarding the voltage measurement, the measurement range and sampling time. The measurement range shall cover the range of 0V to 5V to accommodate all types of battery chemistries including Li-Ions, super capacitors, Lead acid, and NiMH. Typical accuracy for and 0.1% for battery pack voltage up to 600 V [17]. The sampling rate for voltage measurement widely depends on the dynamic behavior but as a rule of thumb, the sampling rate must be at least 20 times higher than the bandwidth of the system [30]. For low-dynamic applications such as stationary energy storage, the sampling rate can be in the range of a minute to 10 seconds. However, for high-dynamic applications such as automotive applications in which the battery current is fluctuating rapidly, the sampling rate of 1 second shall be working fine [57]. The accuracy of measurement heavily depends on the measurement method, which can be categorized into three methods:

1. Linear variable resistor is the simplest approach to measure battery cell voltage, the linear variable resistor found in BMS usually comes in a configuration of a fixed resistor divider or a trimpot resistor. This method is impractical because the accuracy decreases as the number of cells in the string increases. Moreover, the linear variable resistor drains out the battery energy all the time, resulting in less usable capacity.

2. Differential amplifiers [1, 6] are coupled with each battery cell to measure the cell voltage. This method is considered an economical solution for small BMS but not optimal for a large application due to the need for a higher number of components, making it difficult when reconfiguring the gain or the range of voltage measurement because it requires high efforts of soldering work, which is an extremely time-consuming task, especially for a large battery pack.

3. Dedicated BMS ICs are the most common method used in measuring cell voltages in applications where accuracy and power consumption are serious issues, such as automotive applications. The BMS ICs usually provide high accuracy for the voltage measurement over a 40 to 85 °C range for up to 16 cells, together with temperature sensor input ports, adjustable protection voltage and isolated communication. Most of the commercial BMS ICs employ the principle of switched-capacitor sampling techniques which have the ability to simultaneously convert each of the cell voltage into a common signal, so the conversion time per cell is very fast. In addition, the multiplexer can withstand high common-mode voltage up to 60V [60]. These advantages make the BMS ICs the most preferable choice for the implementation of flexible BMS.

For EVs, PHEVs, the battery pack usually composes of a large number of cells connected in series, usually more than 96 cells [31]. So, the conversion time must be fast enough to accommodate the voltage measurement of all cells. In terms of measurement accuracy, the accuracy must have a nominal accuracy of mV for the whole range of 0 V to 5 V to comply with the ASIL-C standard [23]. Thus, it is recommended to use a dedicated IC, which offers fast conversion time, high accuracy, and requires fewer components and less soldering work compared with the other methods.

For HEVs applications, the battery pack used in HEVs is usually a prismatic NiMH cell with 7.2V nominal voltage, which is beyond the range of BMS ICs. So, it is better to use isolated differential amplifier. This method is found in 2009 Toyota Prius [32]. However, to achieve a satisfying accuracy, the isolated amplifier might need a large current while performing sensing [33], typically higher than 4 mA. Which might not be acceptable in automotive application where capacity means travelling distance. Thus, it is suggested to have a transistor to disconnect isolated amplifier when it is not sensing the voltage [34].

For small electric vehicles such as scooters or electric bikes, the number of series-connected cells is usually in the range of 8 cells to 28 cells [31]. So, the conversion time does not have to be so fast, but the measurement accuracy and the measurement range shall be the same as in the EVs or HEVs to support all types of battery chemistry. To achieve the highest flexibility in terms of doing re-configuration without engaging in a lot of soldering work, it is also recommended to use BMS ICs in which the number of cells is configurable in the range of 6 cells to 12 cells, such as LTC6801 from Analog Devices or ISL94212 from Renesas.

2.3. Galvanic Isolation for Interconnection between BMS Module

Several modern commercial BMSs support stackable design, so multiple BMS modules can be vertically added up to monitor a large battery pack. A popular approach is called daisy-chain, which is a bi-directional, differential AC coupled signals which provide high immunity against EMI, by using two-wire cables between two BMS ICs. In the high-voltage stacked configuration, the Daisy chain shall be galvanically isolated for safe operation and for reducing the noises coming into the system. The Daisy-chain isolation can be categorized into 3 types [35, 36] as illustrated below:

1. Capacitive isolation [35] uses a series-connected capacitor and an RC network to provide galvanic isolation between the two BMS modules, the noise reduction is achieved by the RC network acting as low-pass filter. Capacitive isolation is considered a low-cost solution because it consists of only capacitors and resistors. However, the series capacitors are not capable of rejecting common mode noise, so this method is suitable for short-distance interconnections between two BMSs, less than 2 meters, such as on the same PCB.

2. Capacitor and choke isolation [35] a common mode choke is added to enhance common mode noise performance, making it widely used when the distance between 2 BMS modules is greater than 2 m, such as interconnection between 2 PCBs.

3. Isolated SPI [35] is a type of current-source interface using an isolated transformer and two twisted-pair wires as an interconnection between two BMS ICs. This approach effectively eliminates common mode noise out of the communication lines and allows the data transmission rate up to 1 Mbps over a distance longer than 100m. Also, it is able to tolerate a high level of disturbance [36], making it very suitable for automotive applications where electrical noise is high and reliability is the most concern.

Apart from daisy-chain, CAN bus is another popular communication approach in automotive applications due to its high reliability and robustness against electromagnetic noise. CAN bus can also be used to transfer the cells' data between master boards and slave boards in the master/slave configuration [64].

For small vehicles such as electric bikes or scooters, the battery pack usually comes in a small rectangular package composed of battery cells in the range of 8 cells to 28 cells [31], so the distance between each module is not greater than 1 meter. Thus, capacitive isolation is recommended if all of the BMS ICs are integrated on a single PCB, but if there are more than one PCB, capacitor and choke isolation seem to be the best choice.

For EVs, PHEVs, HEVs or even large transportation, the size of battery packs are usually in the range of 24-100 kWh [37], usually consisting of multiple sub-modules connected in series and parallel arrangements to increase capacity and voltage. The total pack size is only around 1m x 2m, which is not a far distance. But the data transmission rate in the automotive application must be at least 1 Mbps [23]. In addition, the distance between each module is probably more than 2 meters, which may result in an EMC problem, especially when the operating environment of EVs has strong electromagnetic interferences. Thus, the most suitable isolation method for this application is isolated SPI.

2.4. Protection Switches

There are mainly two types of protection switches used in battery applications, contactors, and FETs. Contactors generally have high robustness, high tolerance to short circuit current, and do not require gate drivers and heatsink. However, the cost of high-current contactors is very high, might be up to 1,000 USD. The second protection choice is FETs, which are generally soldered on PCBs with a heatsink. The configuration of FET protection can be categorized as high-side and low-side configurations. High-side protection ensures the integrity of grounding and communication stability. However, driving high-side FET needs sophisticated charge pumps to be implemented with BMS ICs, resulting in higher overall cost and power consumption [38]. For low-side protection, the FETs are located at the negative terminal of the battery, so no charge pump is required, resulting in less driving circuit complexity and less power consumption. But low-side FETs might cause unstable communication if the battery ground is not galvanically isolated from the system ground. When the FETs are turned off, the MCU ground will lose connection with the BMS ground, leading to communication instability [20].

For large automotive applications, such as EVs, PHEVs, or HEVs, two contactors are mandatory to meet the safety requirements and level of hazard associated with ISO 26262 [39] and to ensure complete isolation. One contactor shall be installed at the battery-positive pole, another contactor shall be installed at the battery-negative pole. The high-side contactor is controlled by two signals, to ensure that the contactor will not unintendedly turn on during the operation [15]. When selecting a contactor, one must make sure that the contactor shall be able to withstand at least 1.25 times higher than the working voltage and average currents. In addition, the fuses typically used in EVs have a very slow breaking characteristic. So, the contactor shall be able to withstand short-circuit current 16 times higher than the nominal current for 40ms to 100ms [40].

For small vehicle applications such as electric bikes, the battery pack usually comes in a small single module with a nominal capacity of around 8-160 Ah with continuous discharging current around 10-100A [26, 27]. At this current and voltage rating, using contactor might be space-consuming, costly, and inconvenient to be installed inside a small vehicle. Thus, power FETs soldered on PCBs are more preferable to serve as the main protection circuits. If the communication between the microcontroller and BMS ICs is not affected by the breaking ground, or the system has two isolated grounds. Using low-side FETs is the simplest and most cost-effective choice. However, if the ground is unbreakable or the reference signals must be well grounded. Using high-side FETs seems to be the best choice.

2.5. Temperature Acquisition

Battery management for automotive applications must be designed to comply with ASIL-C which states that the BMS module must perform temperature measurements in the range of -40 to +85ºC with a minimum accuracy of ±3ºC [23]. There are two types of temperature sensors widely used in the industrial field and automotive fields. One is thermocouples which work by measuring a small voltage across its junction when the temperature is changed. The measurement range of thermocouples is generally between -200 to 1200ºC, which is suitable for industrial applications, but not suitable for measuring battery temperature. Another approach is to use thermistors, which have high-temperature sensitivity across the range of temperature between -55 to 300ºC [41]. Also, the package of thermistors is relatively small and available in many form factors, making it popular to be embedded in large battery packs at critical points to analyze the overall temperature.

Since there are many factors that influence the thermal behavior of a battery pack such as the charging/discharging rate, mechanical design, type of cooling solution, the arrangement of exhausted fans, etc. So, there is no such "one-size-fits-all" solution to address the thermal issue and to determine the optimal number of temperature sensors required for a particular battery pack of each application. Many works of literature find out the best thermal solution based on simulation, real experiments, or real experience. In [42] the 3-D thermal model 18650 Li-ion battery is constructed based on a non-linear heat transfer equation using FEM simulation to predict the surface temperature distribution along with the high-temperature area. In [43], the author uses a battery simulator and heater to analyze the thermal behavior of battery cells under natural air cooling. In [31], the author roughly estimates the number of temperature sensors based on results from the research and experience but did not mention the optimal placement for those sensors. So, the best practice to find out an optimal number and placement of temperature sensors for a particular battery pack is to use simulation or carry out a real experiment.

2.6. Balancing Algorithm

The main methods widely used for balancing Li-ions cells can be classified into 2 methods, active balancing, and passive balancing. The active balancing method is proven

to be efficient due to low power dissipation, but very costly. So, active balancing usually comes into play only when the battery packs undergo a "gross balancing process", which is an approach to re-balance the whole pack right after the manufacturing process or when the quality of cells used to build the packs is severely unequal [57]. Passive balancing is employed to replenish the unbalanced charge inside battery cells, which occurs because the leakage current of any random cell is not identical to the leakage current of other cells, causing the cells' SOC to end up at a different level compared to the others, as shown in Fig 2. This phenomenon shrinks the battery capacity by limiting the charging capability to the cell having the highest SOC and limiting the discharging capability at the cell having the lowest SOC level. Passive balancing equalizes the level of SOC by bleeding out the excess energy from the high SOC cells in form of balancing current. The optimized value of the balancing current can be calculated from the difference between the maximum and minimum leakage current of each cell, over a balancing time allowed in each automotive application, as shown in Eq. (1)

$$I_{balancing} = \frac{I_{leak,max} - I_{leak,min}}{\text{balancing time per day [hrs]}} \times 24 \text{ [hrs]} \qquad (1)$$
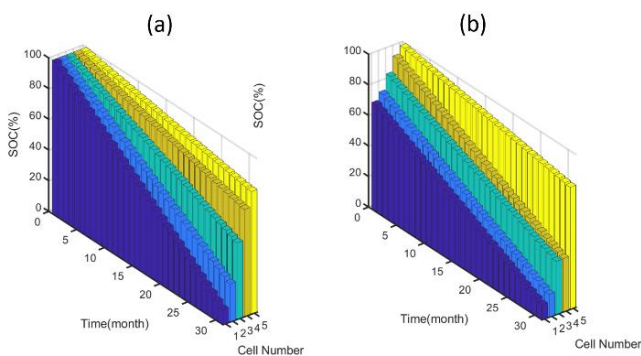

Fig. 2. Unbalance caused by difference of leakage current in each cell (a) start at balanced condition (b) start at unbalanced condition.

Typically, the value of leakage current is not mentioned in the battery datasheet, but Li-ion batteries usually have a typical leakage current of around 1-3% per month (or 0.03-0.1% per day) and for around 30% per month (or 1% per day) for NiMH battery [44]. Assuming that the difference of leakage current ($I_{leak,max}$ - $I_{leak,min}$) in Eq. (1) is assumed to be 0.07% per day for Li-ion batteries and 1% per day for NiMH batteries.

Passive balancing algorithm can be categorized into 3 algorithms, voltage-based algorithm, Full-SOC voltage-based algorithm, and SOC history algorithm.

Voltage-based algorithm [57] determines the starting point and the ending point of the balancing process by measuring the battery terminal voltage and maps it with the SOC-OCV relationship to determine a corresponding SOC value. This algorithm is very simple but not practical because the terminal voltage usually suffers from the

voltage drop across internal battery resistance. Also, some chemistry like LiFePO4 has a very flat curve during the middle region of the SOC-OCV relationship, making it very difficult to differentiate the voltage level during this region.

Full-SOC-based algorithm [57] uses terminal voltage at the end-of-charge to determine which cells need to be balanced. This method can address the issue of the flat region in LiFePO4 since the SOC-OCV curve at the end-of-charge is not flat. However, the end-of-charge usually occurs for a very short time right after the charging process. So, there is only a short time left to perform the balancing. This issue is problematic for some applications in which the charging time is very limited.

SOC-based algorithms [57] use sophisticated battery models to calculate the actual SOC. Then, the SOC difference of each cell is carried out to determine the cells that need to be balanced. The advantage of this method is that the balancing can be performed along the entire charging or discharging cycle, which gives a good flexibility in terms of balancing time and balancing current. The balancing current can be freely chosen as large to shorten the balancing time or can be chosen as small to reduce power dissipation. However, the SOC-based algorithm needs sophisticated battery modeling to extract a precise SOC value in real-time operation, which requires a huge computational power. Thus, SOC based algorithm is not suitable for small applications where the computational power is limited.

For EVs or PHEVs, the type of battery is usually Li-ion cell, which has the difference of leakage current around 0.07% per day and the cell capacity is usually in the range of 15 Ah to 100 Ah [45]. On average, the daily charging time is approximately 12 hours per day, divided into 8 hours for charging and 4 hours for balancing [57]. Thus, the most suitable balancing strategy shall be the full-SOC based algorithm. The recommended balancing current is in the range of 63mA to 420 mA, calculated from Eq. (1).

For HEVs, the battery packs are usually not fully charged or discharged but is kept at around 50%, making the battery pack not prone to over discharge/over charge, so balancing is less demanding in HEVs. However, the battery cells can be balanced once a week by going to 100% SOC and perform full-SOC balancing [57] for 10 minutes. The typical capacity of each HEVs cell is around 6-10 Ah [32]. So, the most suitable strategy is performing full-SOC-based balancing for 10 minutes, once a week with a balancing current of 175-300 mA, determined from Eq. (1).

For small vehicles like E-bikes, scooter, the standard battery capacity is between 8 and 15 Ah [26], so the maximum difference of leakage current is around 15 mA/day. The SOC of the cells is usually kept in the range of 30% to 70% during the driving [57], so the battery cells are rarely experiencing the overcharge/over-discharge situation, same as in HEVs. Thus, the balancing process can be performed once a week for 10 minutes by going to

100% SOC [57] with a balancing current of 235-450 mA, determined from Eq. (1).

To increase the flexibility of balancing circuit, it is recommended to use external balancing transistors or FETs, to enable the use of high balancing currents and to support a wide range of battery capacity. All in all, the recommended implementation of flexible BMS based on 6 crucial aspects, has been summarized in Table 2. The sign (++) indicates this configuration is highly recommended, whereas (+) is moderately recommended and (o) is not recommended.

Table 2. Recommended implementation of flexible BMS based on 6 crucial aspects.

Vehicle Types	Current measurement			Voltage Measurement		Interconnection			Protection Switches		Balancing algorithm			Balancing Current (mA)
	Shunt	Kelvin Shunt	Hall Sensor	Differential amplifiers	Dedicated ICs	Capacitive isolation	Capacitor and choke isolation	Isolated SPI	High side	Low side	Voltage based	Full SOC based	SOC base	
PHEV EVs	o	++	+	o	++	o	+	++	++ (Both sides are required)		o	++	+	63-420
HEVs	o	++	+	++	o	o	+	++			o	++	+	175-300
Small Vehicle	++	+	o	+	+	++	+	+	+	++	+	++	+	235-450

It is worth to mention that, the control of passive balancing can be implemented by a number of ways such as in [62] the balancing current of a modular BMS is controlled by adjusting the PWM duty cycle with a fixed resistor. Similar modular BMS is found in [61], where the linear region of a MOSFET is used as the balancing resistors. As a result, the balancing current can be precisely controlled in a real-time by adjusting the amplitude of V_{gs} of the MOSFET. Another FET-based balancing is found in [63], where a balancing scheme can perform both passive and active balancing by using a parallel connection of NMOS and PMOS. The linear region of an NMOS is used as a balancing resistor, and the PMOS is used to control the charging process. This design is flexible and economical because it can perform both passive and active balancing by using only a single circuit. In [65], A BMS for 13S2P 18650 Li-ions for e-bike was developed based on ESP32 WiFi module to wirelessly control the charging and balancing processes. During the charging, parallel resistors are connected to the first 4 cells with the highest voltage to ensure that all cells' voltage shall be equalized. The result shows that all of the cell voltage became equalized within just 60 minutes.

3. Battery Modelling and SOC Estimation Algorithm

3.1. Battery Modelling

There are two techniques vastly used to implement battery modeling in automotive applications, electrochemical modelling method and equivalent circuit modelling (ECM) method [46]. ECM method is considered as a cost-effective solution for onboard BMS due to the ease of parameter identification and their structural simplicity. There are several types of ECM models used in BMS application, such as first order model, 2-RC model, third-order and n-RC model [30]. The higher order the model is, the higher estimation accuracy the model can provide, but at the expense of higher computational power. Most of the literature published recently usually use a second-order model as the optimal trade-off between computational time and accuracy [47, 48]. The processor used in these works are powerful desktop CPUs, but the processing units found in most BMSs are usually a small-scale to middle-scale microcontroller, which is much less powerful than the desktop CPUs. Therefore, determining the computational time and resources usage based on CPUs is not practical for the implementation of onboard BMSs.

In this work, the comparison of 1-RC, 2-RC and 3-RC ECM under Luenberger observer (LO) and Extended Kalman filter (EKF) have been carried out based on a 32-bit Arm Cortex microcontroller to find out the optimal trade of between computational time and estimation accuracy. The battery model illustrated in Fig. 3 mainly consists of three parts [30]: (1) parallel RC branches which represent the short-time and long-time polarization and concentration effect inside the battery. (2) ohmic resistance which represents an abrupt change of battery terminal voltage. (3) a DC voltage source representing open-circuit voltage as a function of SOC.

In order to complete the n-order ECM, the time-varying internal parameters including series resistance polarization resistance and polarization capacitance need to be identified. Starting by deriving the Laplace transform of n-order ECM and applying Kirchhoff's voltage law, Eq. (2) is obtained as
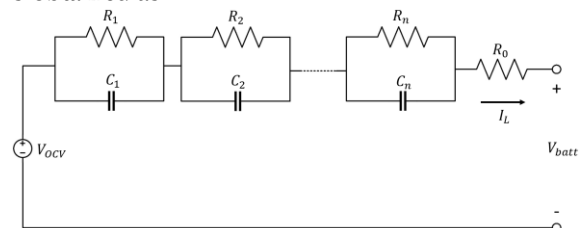

Fig. 3. n-order battery electrical circuit model.

$$V_{batt}(s) = V_{OCV}(s) - I_L(s)\left(R_0 + \frac{R_1}{1+R_1C_1s} + \frac{R_2}{1+R_2C_2s} + \frac{R_3}{1+R_3C_3s} + \cdots + \frac{R_n}{1+R_nC_ns}\right) \quad (2)$$

where $V_{batt}(s)$, $V_{OCV}(s)$ and $I_L(s)$ are the Laplace transform of battery terminal voltage, open-circuit voltage and battery current, respectively, n denotes the number of RC circuits. This continuous transfer function shall be converted into a discrete transfer function by using bi-linear transformation, replacing the term $s = \frac{2}{T_s}\frac{1-z^{-1}}{1-z^{-1}}$. Then, the discrete form of ECM equation can be achieved as Eq (3).

$$\begin{aligned}(z^{-n}+a_1z^{-n+1}+\ldots+a_{n-1}z^{-1}+a_n)V_{batt}\\ -(z^{-n}+a_1z^{-n+1}+\ldots+a_{n-1}z^{-1}+a_n)V_{OCV}\\ =(z^{-n}+b_1z^{-n+1}+\ldots+b_{n-1}z^{-1}+b_n)I_L\end{aligned} \quad (3)$$

Since the term V_{OCV} is a state-dependent variable, which needs to be changed to a time-independent variable by considering the complete OCV equation in microscopic level with respect to temperature and SOH over time, as described in Eq. (4) [49]

$$\dot{V}_{OCV} = \dot{V}_{OCV}(SOC, T, h) = \frac{\partial V_{ocv}}{\partial SoC}\frac{\partial SoC}{\partial t} + \frac{\partial V_{ocv}}{\partial T}\frac{\partial T}{\partial t} + \frac{\partial V_{ocv}}{\partial h}\frac{\partial h}{\partial t} \quad (4)$$

Equation (4) can be further simplified to $\dot{V}_{OCV} \approx 0$ by considering that a battery cell is being charged/discharged at 10C (generally less than this value at most time) with a sampling rate of 1s. The approximated SOC variation at each step is $\frac{\partial SOC}{\partial t} \approx$ -0.277%, which is small enough to holds the assumption of $\frac{\partial SOC}{\partial t} \approx 0$. Moreover, for a battery cell with a good BMS, the battery cell temperature shall be controlled and regulated by a proper cooling or heating system to avoid a rapid temperature change, which might cause a thermal runaway situation. Thus, $\frac{\partial T}{\partial t} \approx 0$ holds during normal operating condition. In addition, when considering only a short time usage history of a battery cell in a normal operating condition (no abusive use, over charge/discharge), the SOH of the cell does not change much, so the assumption $\frac{\partial h}{\partial t} \approx 0$ is valid for a short time usage. By considering these assumptions, the term V_{OCV} is no longer time-dependent and becomes just an unknown parameter, which shall be included in the unknown matrix θ_k. Thus, Eq. (3) is further simplified as shown in Eq. (5)

$$\begin{aligned}(z^{-n} + a_1z^{-n+1} + \cdots + a_{n-1}z^{-1} + a_n)V_{batt} - \alpha V_{OCV} = \\ (z^{-n} + b_1z^{-n+1} + \cdots + b_{n-1}z^{-1} + b_n)I_L\end{aligned} \quad (5)$$

where α is a constant term, this discrete Laplace transform shall be used to identify all internal parameters by using the process of RLS which is summarized in Algorithm 1

To verify the estimation results, the Hybrid Pulse Power Characterization (HPPC) test are performed to extract the battery internal parameters. The HPPC test is made up of multiple repetitive 100 second charge/discharge cycles at 1C to 6C current rating, then

followed by 400 second resting times. These cycles are repeated at the level of SOC from 100% down to 0%. The voltage and current characteristic of the HPPC test are shown in Fig. 4(a) and Fig. 4(b), respectively.
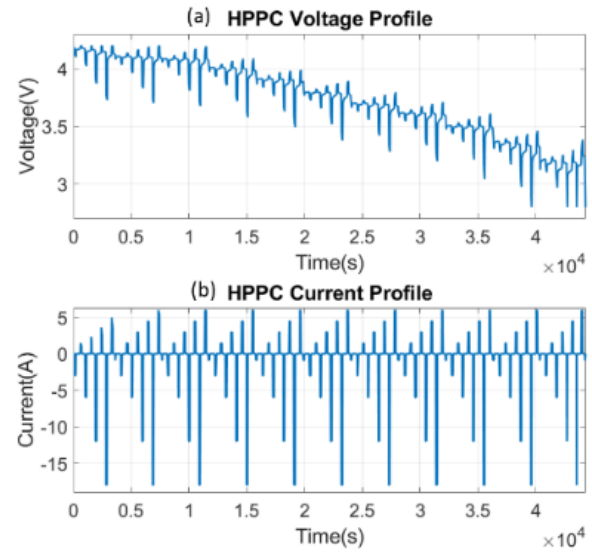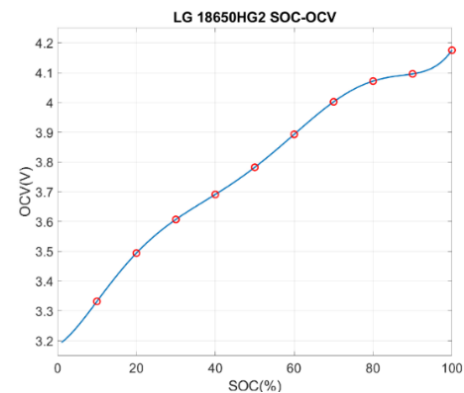

Fig. 4. HPPC profile (a) voltage profile (b) current profile.

The dataset of HPPC test was carried out by McMaster University, Ontario, Canada [53] using LG 18650HG2 NMC cell. The relationship between SOC and OCV of this cell is shown as in Fig. 5.

OCV = $(4.0114e-11)*(SOC)^6 - (1.1714e-8)*(SOC)^5 + (1.2618e-6)*(SOC)^4 - (6.0708e-5)*(SOC)^3 + 0.0011755*(SOC)^2 + 0.0079*(SOC)^1 + 3.1845$

Fig. 5. OCV-SOC relationship of LG 18650HG2.

When the cell is discharged with a pulse current, the equivalent series resistance (R_0) and the time constant (τ) of the battery cell can be extracted. Since R_0 causes the terminal voltage to suddenly drop when the cell is being discharged, and suddenly rise back to a certain value when discharging pulse is removed. So, by considering the abrupt change of terminal voltage V_0 the value of R_0 can be calculated as Eq. (6):

$$R_0 = \frac{\Delta V_0}{\Delta I_L} \quad (6)$$

Algorithm 1: Recursive Least Square algorithm	
0	Initializing the parameter vector at k = 0 $\hat{\theta}_0 = (0\ 0\ 0\ 0\ 0)^T$ $P_0 = (\varphi_0^T \varphi_0)^{-1}$
1	Construct unknown vector θ_k and input vector φ_k $\theta_k = [\alpha V_{OCV}\ a_1\ a_2\ a_3 \dots a_n\ b_1\ b_2\ b_3 \dots b_n]$ $\varphi_k = [1\ -V_{batt}(k-1)\ -V_{batt}(k-2)\ -\dots-V_{batt}(k-n)\ I_L(k)\ I_L(k-1)\ I_L(k-2)\ I_L(k-3)\ ]^T$
2	Update the covariance matrix P: $P_{k+1} = P_k - \frac{P_k \varphi_{k+1} \varphi_{k+1}^T P_k}{1 + \varphi_{k+1}^T P_k \varphi_{k+1}}$
3	Calculate unknown vector $\hat{\theta}_k$: $\hat{\theta}_k = (\varphi_k^T \varphi_k)^{-1} \varphi_k^T V_{batt,k}$ where $V_{batt,k} = [V_{batt,k-1}, V_{batt,k-2}, \dots, V_{batt,k-n}]^T$; n is total number of data samples.
4	Calculate the gain vector: $L_k = P_k \varphi_k = P_{k-1}\varphi_k(I + \varphi_k^T P_{k-1}\varphi_k)^{-1}$
5	Update unknown vector: $\hat{\theta}_{k+1} = \hat{\theta}_k + L_k(V_{batt,k+1} - \varphi_k^T \hat{\theta}_k)$

After the discharging pulse is gone, the cell goes into a so-called "diffusion period", which causes the terminal voltage to slowly recover its amplitude back to its steady-state OCV. The diffusion voltage is changing as an exponential function which can be described as Eq. (7)

$$\Delta V_{terminal} = V_{ocv,steady}\left(1 - e^{-\frac{t}{\tau}}\right) \qquad (7)$$

where $V_{ocv,steady}$ is the value of steady-state OCV at each level of SOC, obtained from the SOC-OCV curve shown in Fig. 5.

An example of R_0 and τ calculation was taken from the HPPC test at the point of SOC 90% as shown in Fig. 6, the cell was discharged first with an 18A (6C) pulse current for 100 seconds, then rested for 400 seconds, allowing the cell to enter the diffusion region. So, the values of R_0 and τ at a particular level of SOC ($R_0|_{SOC}$ and $\tau|_{SOC}$) can be calculated as Eq. (8) and Eq. (9), respectively.
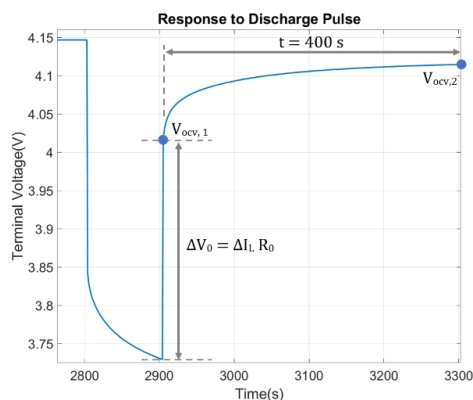

Fig. 6. Response to the 18A (6C) discharge pulse of HPPC voltage profile .

$$R_0|_{SOC} = \frac{\Delta V_0|_{SOC}}{18\ A} \qquad (8)$$

$$\tau|_{SOC} = \frac{-400\ s}{\ln\left(1 - \frac{V_{ocv,2} - V_{ocv,1}}{V_{ocv,steady}}\right)} \qquad (9)$$

The values of R_0 and τ with respect to SOC level, ranging from 100% down to 0% can be calculated as shown in Table 3. These values shall be used as the reference R_0 and τ to compare with the estimated results obtained from the recursive least square estimation. In Fig. 7(a), Fig. 7(c) and Fig. 7(d) show the estimated transient voltage response obtained from the HPPC test under all ECM levels. It can be observed that the abrupt change of 3-RC model can best fit with the reference SOC value, and also closest to the reference time constant and reference ohmic resistance obtained from Table 3, whereas the 2-RC model offers a moderate fit. Figure 7(b) shows that the error produced from 1-RC is in the range of 1.5-2% when SOC is in the range of 80-100% and when the SOC is near to 0%. Whereas, the error of 2-RC and 3-RC are maintained close to 1%.
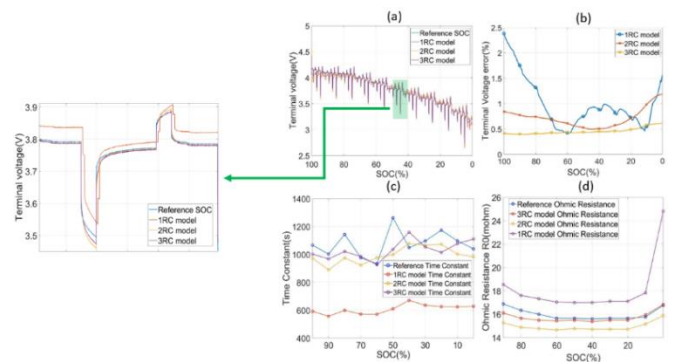

Fig. 7. HPPC estimation results of each ECM level according to the change of SOC (a) estimated terminal voltage, (b) estimated terminal voltage error, (c) time constant, (d) ohmic resistance.

Thus, having just 1-RC might not enough to produce a satisfactory estimated result, but might require at least 2-RC for a good estimation accuracy. The ohmic resistance obtained from all ECM levels are around 20 mΩ, and it is kept constant during the SOC of 90% to 0% as shown in Fig. 7(d). This indicates that the ohmic resistance is not affected much by the SOC level and the complexity of ECM model.

Table 3. Calculated equivalent series resistance (R_0) and time constant (τ) obtained from the HPPC profile, from 100% SOC down to 0% SOC.

SOC (%)	ΔV_0 (V)	ΔI_L (A)	Calculated R_0 (mΩ)	$V_{ocv,1}$ (V)	$V_{ocv,2}$ (V)	$V_{ocv,steady}$ (V)	Calculated τ (s)
100%				4.016	4.115	4.160	1067.57
90%	0.304		16.888	3.984	4.082	4.130	1003.41
80%	0.294		16.333	3.957	4.055	4.096	1144.47
70%	0.288		16.000	3.858	3.949	3.995	977.71
60%	0.282		15.666	3.771	3.857	3.903	933.58
50%	0.282	18	15.666	3.655	3.757	3.795	1263.15
40%	0.281		15.611	3.558	3.655	3.700	1049.55
30%	0.282		15.666	3.479	3.570	3.610	1097.88
20%	0.282		15.666	3.329	3.472	3.530	1174.88
10%	0.284		15.777	3.107	3.264	3.333	1098.03
0%	0.302		16.777	3.101	3.165	3.195	1040.55

3.2. Discrete State-space Representation of the ECM Battery Model

In order to perform SOC estimation, it is necessary to realize the discrete state-space representation of the battery, by applying the Kirchhoff's voltage law on a 3-RC ECM model shown in Fig. 3, Eq. (10) is obtained as

$$V_{batt}(t) = V_{OCV}(SOC) - V_1(t) - V_2(t) - V_3(t) - R_0 I_L(t) \qquad (10)$$

where $V_{OCV}(SOC)$ is the open-circuit voltage as a function of SOC. V_1, V_2, V_3 are the voltage across each RC circuit, which is defined by its derivative as

$$\dot{V}_{RC}(t) = -\frac{V_{RC}(t)}{RC} + \frac{I_L(t)}{C} \qquad (11)$$

And the relationship between the level of SOC and the load current $I_L(t)$ can be described as in Eq. (12).

$$SOC(t) = SOC(0) - \int_0^{t'} \frac{I_L(t)}{Q_n} dt \qquad (12)$$

where Q_n is the nominal capacity of the battery, $SOC(0)$ is the initial value of SOC. By considering Eq. (10) to Eq. (12), the continuous state equation of ECM model can be expressed as Eq. (13) and Eq. (14)

$$\dot{x}(t) = A_{con}x(t) + B_{con}u(t) \qquad (13)$$

$$y(t) = V_{OCV}(SOC) - V_1(t) - V_2(t) - V_3(t) - R_0 u(t) \qquad (14)$$

where $u(t) = I_L(t)$, $x(t) = [SOC, V_1, V_2, V_3]^T$ and

$$\begin{cases} A_{con} = \begin{bmatrix} 1 & 0 & 0 & 0 \\ 0 & -\dfrac{1}{R_1 C_1} & 0 & 0 \\ 0 & 0 & -\dfrac{1}{R_2 C_2} & 0 \\ 0 & 0 & 0 & -\dfrac{1}{R_3 C_3} \end{bmatrix} \\ B_{con} = \left[\dfrac{1}{Q_n}, \dfrac{1}{C_1}, \dfrac{1}{C_2}, \dfrac{1}{C_3}\right]^T \end{cases}$$

Then, these continuous state-space equations shall be transformed into discrete state-space equations to be used with real-time SOC estimation, by using discretization of continuous system, we will get discrete state-space equations as shown in Eq. (15). Please note that the exponential terms in matrix A_{dis} and B_{dis} can be further simplified by using the Taylor expansion, $e^x \approx 1 + \frac{x}{1!} + \frac{x^2}{2!} + \cdots$.

$$x_{k+1} = A_{dis}x_k + B_{dis}u_k \qquad (15)$$

where A_{dis} and B_{dis} are the discrete state-space matrices, with the sampling time T_s.

$$\begin{cases} A_{dis} = \begin{bmatrix} 1 & 0 & 0 & 0 \\ 0 & e^{-\frac{T_s}{R_1 C_1}} & 0 & 0 \\ 0 & 0 & e^{-\frac{T_s}{R_2 C_2}} & 0 \\ 0 & 0 & 0 & e^{-\frac{T_s}{R_3 C_3}} \end{bmatrix} \\ B_{dis} = \left[\dfrac{T_s}{Q_n} \quad R_1\left(1 - e^{-\frac{T_s}{R_1 C_1}}\right) \quad R_2\left(1 - e^{-\frac{T_s}{R_2 C_2}}\right) \quad R_3\left(1 - e^{-\frac{T_s}{R_3 C_3}}\right)\right]^T \end{cases}$$

Since the time constant of ECM model is usually much larger than the sampling time ($R_1 C_1, R_2 C_2, R_3 C_3 \ggg T_s$), so the exponential term can be further approximated using Taylor series expansion $e^x \approx 1 + x$

$$\begin{cases} A_{dis} \approx \begin{bmatrix} 1 & 0 & 0 & 0 \\ 0 & 1 - \dfrac{T_s}{R_1 C_1} & 0 & 0 \\ 0 & 0 & 1 - \dfrac{T_s}{R_2 C_2} & 0 \\ 0 & 0 & 0 & 1 - \dfrac{T_s}{R_3 C_3} \end{bmatrix} \\ B_{dis} \approx \left[\dfrac{T_s}{Q_n} \quad \dfrac{T_s}{C_1} \quad \dfrac{T_s}{C_2} \quad \dfrac{T_s}{C_3}\right]^T \end{cases}$$

Algorithm 2: Extended Kalman Filter algorithm	
	Initialize the values of matrix Q_k, R_k and error covariance matrix P_0 and $\hat{x}_0$
Step 1: Initialization Step	$\hat{x}_0 = [1\ 0\ 0\ 0]$, $P_0 = \begin{bmatrix} 1 & 0 & 0 & 0 \\ 0 & 1 & 0 & 0 \\ 0 & 0 & 1 & 0 \\ 0 & 0 & 0 & 1 \end{bmatrix}$, $R_k = 0.27\ \text{mV}$, $Q_k \approx 0$
Step 2: Prediction Step	Estimate the next state variables $\hat{x}_{k+1} = A_k \hat{x}_k + B_k u_k$
Step 3: Calculate covariance matrix P_k	$P_k = A_k P_k A_k^T + Q_k$
Step 4: Correction Step	Update Kalman gain $L_k = P_{k+1} C_k^T [C_k P_{k+1} C_k^T + R_k]^{-1}$
Step 5: Update next state	Update the next state variables $x_{k+1} = \hat{x}_{k+1} + L_k[y_k - C_k \hat{x}_{k+1} - D_k u_k]$ Update the covariance matrix $P_{k+1} = (I - L_k C_k) P_k$

3.3. SOC Estimation Based on Extended Kalman Filter (EKF)

Extended Kalman Filter (EKF) is an improved version of Kalman filter methods (KF), which is designed to handle a state estimation on nonlinear systems, especially in battery models where the relationship between SOC and OCV exhibits a strong nonlinear characteristic, by linearizing the mean and covariance vectors of the battery model. The EKF takes into account the previous state of SOC, and polarization voltage to generate the optimal estimated values based on the measurement noises and the new incoming inputs. The discrete nonlinear state equation of the ECM model can be represented as shown in Eq. (16) and Eq. (17)

$$x_{k+1} = f(x_k, u_k) + w_k = A_{dis} x_k + B_{dis} u_k + w_k \quad (16)$$

$$y_k = h(x_k, u_k) + v_k \quad (17)$$

where

$$h(x_k, u_k) = V_{OCV}(SOC_k) - V_{1,k} - V_{2,k} - V_{3,k} - R_{0,k} I_{L,k}$$

A_{dis}, B_{dis} are the discrete state-space matrices obtained from section 3.2. w_k and v_k are the zero-mean process noise and measurement noise with the covariance of Q_k and R_k $\left(w_k \sim (0, Q_k), v_k \sim (0, R_k)\right)$, respectively. The first step of EKF algorithm is to linearize of the state equations Eq. (16) and Eq. (17) around the operating point by calculating the Jacobian matrices A_k and C_k of each sampling, as shown in Eq. (18)

$$\begin{cases} A_k = \left.\frac{\partial f(x_k, u_k)}{\partial x_k}\right|_{x_k = x_k^+} = A_{dis} \\ B_k = B_{dis} = \left[\frac{T_s}{Q_n} \quad \frac{T_s}{C_1} \quad \frac{T_s}{C_2} \quad \frac{T_s}{C_3}\right]^T \\ C_k = \left.\frac{\partial h(x_k, u_k)}{\partial x_k}\right|_{x_k = x_k^+} = \left[\left.\frac{\partial V_{OCV}}{\partial SOC}\right|_{SOC_k} \quad -1 \quad -1 \quad -1\right] \\ D_k = [R_0] \end{cases} \quad (18)$$

The term $\left.\frac{\partial V_{OCV}}{\partial SOC}\right|_{SOC_k}$ is obtained from the slope of SOC-OCV curve in Fig. 5. The values of R_1C_1, R_2C_2,

R_3C_3 and R_0 inside the matrix A_k B_k and D_k are obtained from the parameter estimation in the section 3.1.

Next, the EKF requires the initialization of $\hat{x}_0$, Q_k, R_k and P_0. In this study, since all of the tests are started with 100% SOC, so $\hat{x}_0 = [1\ 0\ 0\ 0]$. There is no disturbance in the estimation process, so the process noise matrix Q_k is assumed to be zero. The covariance of voltage measurement noise R_k is approximately 0.27 mV, which is obtained from the 16-bits ADC of RA2A1 MCU, which is used as the voltage sensor. The error covariance matrix P_0 is first assumed to be an identity matrix. The summary of EKF process is described in the algorithm 2.

3.4. SOC Estimation Based on Luenberger Observer

Luenberger observer (LO) [51] is a state estimator widely used to predict state variables of a given linear dynamic system because it has a good estimation accuracy and low complexity. The structure of LO is constructed from the summation of the parameters obtained from the typical state equation and a correction term, which can be written as Eq. (19) and Eq. (20).

$$\hat{x}_{k+1} = A_k \hat{x}_k + B_k u_k + L(y_k - \hat{y}) \quad (19)$$

$$\hat{y}_k = C_k \hat{x}_k + D_k u_k \quad (20)$$

where L is the observer gain vector and $L(y_k - \hat{y})$ is the correction term which defines the dynamic behaviour of the observer. A_k, B_k, C_k and D_k are the linear state matrices mentioned in Eq. (18). To satisfy good estimation accuracy and dynamic performance, the observer gain L shall be selected in such a way that makes the eigenvalues of $A_k - LC_k$ are asymptotically stable and located inside a left-half plane unit circle to guarantee that the observer error converges to zero for any initial condition. The observer gain L shall be selected using the direct-substitution approach [52], by assuming that the desired poles are placed at ω_1, ω_2,..., ω_n which shall be selected by considering dynamic performance and stability. The observer gain matrix L can be determined as shown in Eq. (21)

$$L = [L_1 \; L_2 \; ... \; L_n]^T \qquad (21)$$

$$eig(sI - (A_k - LC_k)) = (s - \omega_1)(s - \omega_2)...(s - \omega_n) \qquad (22)$$

By equating the coefficients on both sides of Eq. (22), the values of observer gain L can be determined.

The key point in selecting the location of ω_1, ω_2 and ω_3 is that we need ω_1 to be the significant pole, which determines the response of the system. The other poles must be insignificant to make sure that they will not have an influence on the desired response. So, by setting ω_1 to be 10 times smaller than ω_2. ω_1 will become the dominant pole located at the desired location poles.

3.5. SOC Estimation Validation from Standard Driving Cycles

To validate the performance of each level of ECM models under LO or EKF, numerous standard driving cycles such as California Unified cycle (LA92) which is a chassis dynamometer driving schedule for light-duty vehicles, Urban Dynamometer Driving Schedule (UDDS) which represents the certification of light-duty and passenger vehicles, and US06 which represents aggressive driving, or high-speed driving behavior, are required to evaluate the accuracy and robustness of the models. The dataset of these driving cycles was prepared by McMaster University, Ontario, Canada [53], using NMC cell from LG. The battery cell was initially at 100% SOC before undergoing each test, then the cell was charged/discharged at different C rates until the SOC reached 5%. Apart from the standard driving, a special case of pulse discharge of LiFePO$_4$ battery cell was also carried out to be used as a test case. This is because the OCV-SOC relationship of LiFePO$_4$ is very flat during the middle region, making the SOC prediction between the SOC of 30% to 80% become a challenging task. The battery cell used in this study is HDCF26650 from TiraThai, whose nominal voltage is 3.2V and nominal capacity 4000 mAh. The sampling time was set at 1 second ($T_s = 1$ s).

In the experiment, the reference SOC was carried out through the noiseless coulomb-counting method. Then, the value of estimated SOC values obtained from 1-RC, 2-RC, and 3-RC under the standard driving datasets UDDS, US06, LA92 and a pulse discharging of LiFePO$_4$ were carried out and compared with the reference SOC, which was conducted through coulomb-counting method. Fig. 10 shows the current/time curves of the estimation results of these driving cycles. It is observed that all algorithms under all levels of ECM follow the reference SOC value. However, the closest results to the reference SOC value are obtained with 3-RC ECM.

In case of pulse discharging of LiFePO$_4$, it can be seen that the largest deviation of results from the reference SOC value occurred during the SOC of 40% to 80%, because this region is typically the flat region of LiFePO$_4$.

The estimation errors are illustrated in the form of a statistical box plot as shown in Fig. 9(a) which represents the distribution of SOC error of UDDS, LA92, US06, and discharge pulse under 1-RC, 2-RC, and 3-RC with EKF and LO algorithm, respectively. The central mark indicates the median value, the bottom and top marks of the box indicate the and percentiles (IQR interval) of the distribution. Considering the position of each box, the typical tendency of IQR interval of the 1-RC model falls into the range of 2.8% to 5% for both EKF and LO algorithms. Followed by the 2-RC model and 3-RC model whose IQR intervals fall in the range of around 1.5% to 3.5% and 1.3% to 3.4%, for both algorithms, respectively.

It is worth mentioning that, the 3-RC model generally gives a slightly lower percentile SOC error, and also a slightly shorter IQR interval compared with the 2-RC model. However, in the case of the US06 driving cycle, the IQR interval of the 2-RC model is almost identical to the IQR interval of the 3-RC model. Thus, these outcomes can be used to make a generalization that the change from the 2-RC model to the 3-RC model does not provide a significant improvement in SOC estimation, for both EKF and LO algorithms. In the case of discharge pulse, the IQR interval and the percentile of SOC error were significantly decreased when the model was changed from a 1-RC model to a 2-RC model and even got lower the model was changed from 2-RC to 3-RC. In the 1-RC model, the error produced by the EKF was in the range of 3.5% to 4.2% for the EKF and 4.2% to 5% found in LO.

Apart from the IQR distribution, the root means square error (RMSE) [54] of all driving cycles under each level of ECM have been calculated as another performance evaluation criteria, as shown in Fig. 9(b). It can be observed that the average RMSE of 1-RC ECM is approximately 3.5% for NMC cell under all standard driving cycles, and 4.5% for LiFePO$_4$ under the pulse discharging.
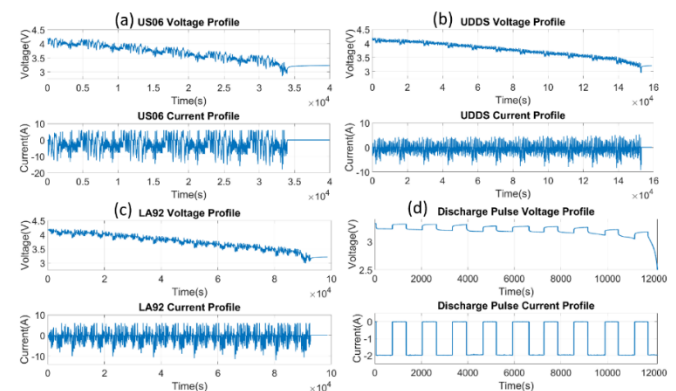

Fig. 8. Voltage and Current profile of standard driving cycles (a) US06, (b) UDDS, and (c) LA92, (d) Pulse discharge of LiFePO$_4$
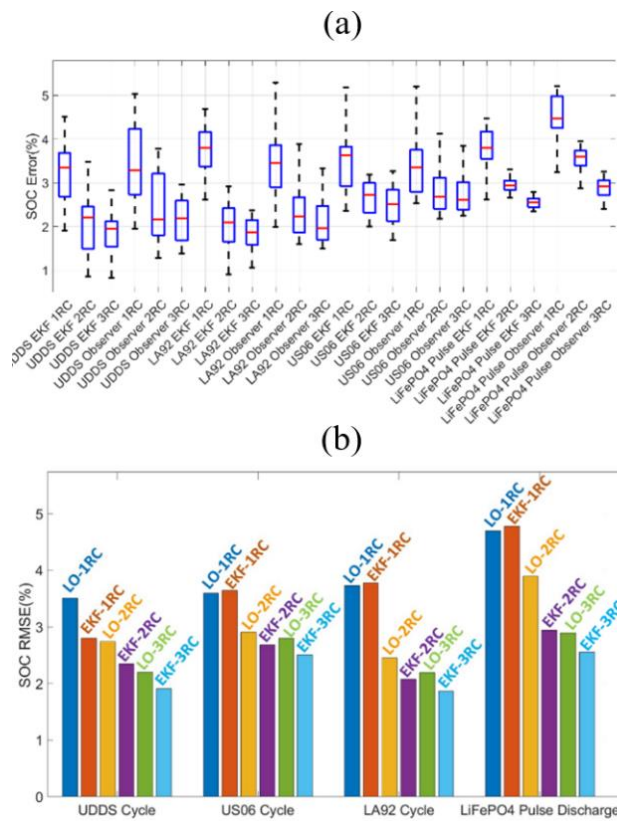
Fig. 9. SOC estimation error of under 1-RC to 3-RC ECM model (a) statistical box plots, (b) Root-mean-square error cycle and LiFePO$_4$ discharge

When the model is changed to 2-RC ECM, the RMSE decreased to around 2.0% for the NMC cell and to 2.6% for the LiFePO$_4$ cell. These decreases are considered as significant changes, especially in the case of 2-RC EKF in which the RMSE decreased from 4.6% to 2.6%. However, there was no significant change in the RMSE values between 2-RC ECM and 3-RC, which gives only around 0.5% to 1% decrease in RMSE.

3.6. Dynamic Convergence

Typically, when a BMS is plugged into a battery cell, the process of SOC estimation begins by initializing a SOC value at time t = 0, either by using a look-up table or open-circuit voltage (OCV). If the value of SOC is not initialized correctly or the data is corrupted, the estimated SOC value will deviate from its correct value. So, the estimation algorithm must be able to quickly converge from the wrong SOC to its correct value. To achieve a satisfying convergence response, the desired observer eigenvalues shall be set to balance between convergence speed and noise level [55, 58], too fast response might lead to the loss of accuracy and unacceptable level of noise [56]. The slowest response of the NMC battery cell is approximately 950 seconds, found in the 3-RC ECM model as shown in Fig. 11(c). This value shall be used to realize the optimized range of poles by varying the speed of pole from 1 time to 20 times faster than the slowest response. The LO gain is

determined by Eq. (21) and Eq. (22) and the evaluation of dynamic performance is analysed by discharging a battery cell with a constant current from 100% SOC to 0% SOC. Then, the initial SOC value was set incorrectly at 50% at t =0.

It can be observed from Fig. 11(a) and Fig. 11(b) that, both LO and EKF have the ability to converge the incorrect SOC value back to its correct value. In terms of dynamic robustness, it can be seen in Fig. 11(a) that the noise level was insignificant when the pole was set equal to the system pole (1x pole), but it took more than 3,000s to reach the reference SOC with an error of around 1%. When the pole is set to be 20 times faster than the system pole (20x pole), the convergence time is reduced to only around 200s, but the noise becomes very obvious, and the terminal error is more than 5% due to the accumulated noise. When comparing LO with EKF, the convergence time of EKF is comparable to the LO when the pole was set at 5 times faster than the open-loop pole. However, the noise level of LO is almost as twice as the EKF (2.35% vs 1.48%) as shown in Fig. 11(b). Since the accuracy of SOC estimation must fall in the range of 3–5% for automotive applications, the observer poles in the range of 2 to 5 times faster than the system poles are recommended to achieve a fast convergence while minimizing the effect of disturbance on the system.

3.7. Computational Time

Apart from the SOC estimation accuracy and dynamic performance, computational time is another important point for evaluating the performance of the SOC estimation algorithm. This time indicates the number of the battery cell in which a microcontroller can handle within a defined sampling interval. In this section, the computational time of all ECM models with EKF and LO are compared to find out the optimal trade-off between the accuracy and computational time. The microcontroller used in this study is RA2A1 32-bit 48 MHz Arm Cortex M23 from Renesas, the total computational time of each level of ECM with LO/EKF is determined as shown in Table 4.

Table 4. Computational time and average RSME of each level of ECM under LO and EKF algorithm.

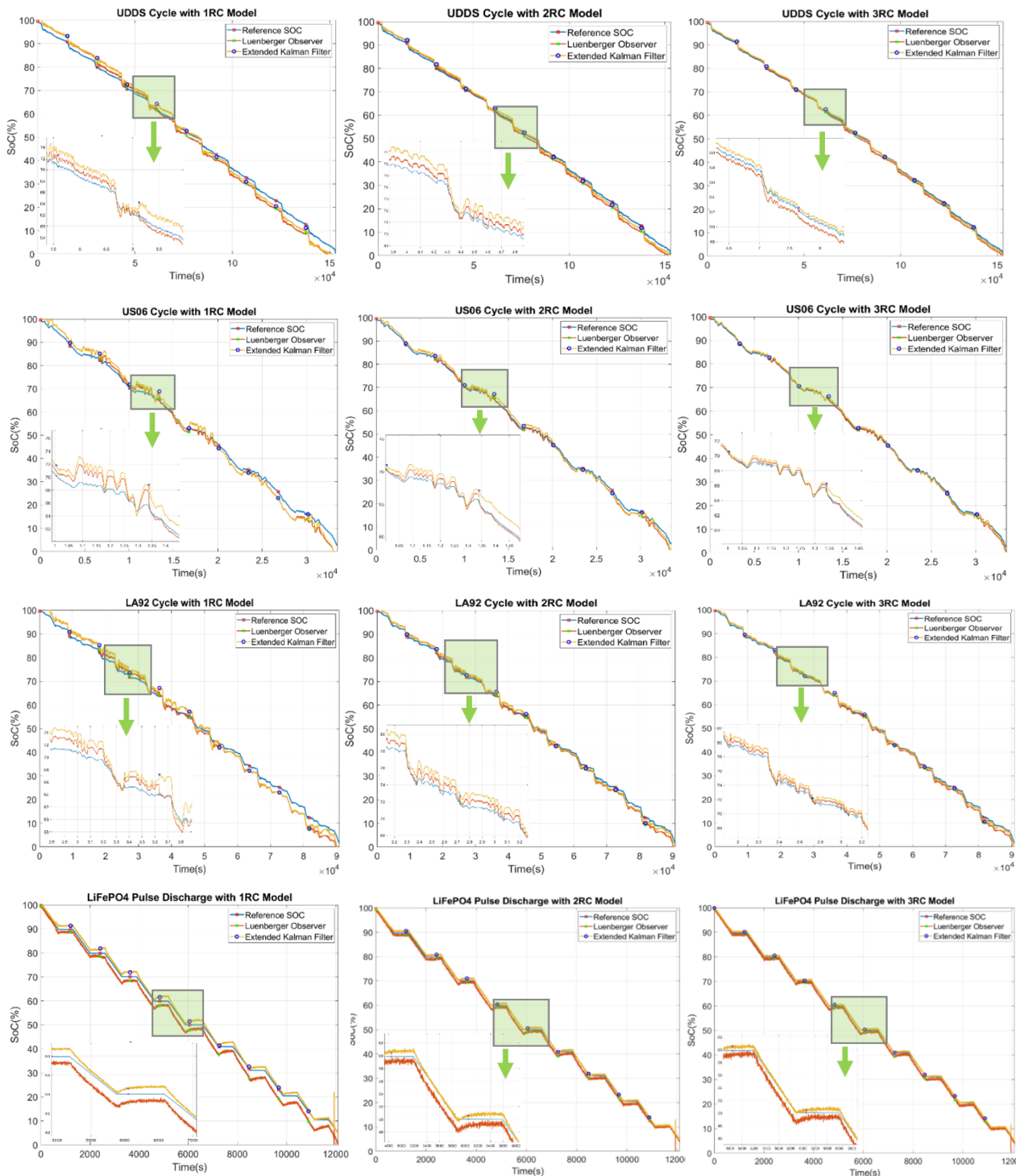| Configuration	Computational Time (ms)	Average RMSE (%)
LO 1-RC	1.19	3.88
LO 2-RC	2.58	2.83
LO 3-RC	4.48	2.53
EKF 1-RC	1.43	3.75
EKF 2-RC	2.58	2.42
EKF 3-RC	4.86	2.21

Fig. 10. SOC estimation curves of LO and EKF under 3 levels of ECM for UDDS, US06, LA92 driving cycle and LiFePO₄ discharge.
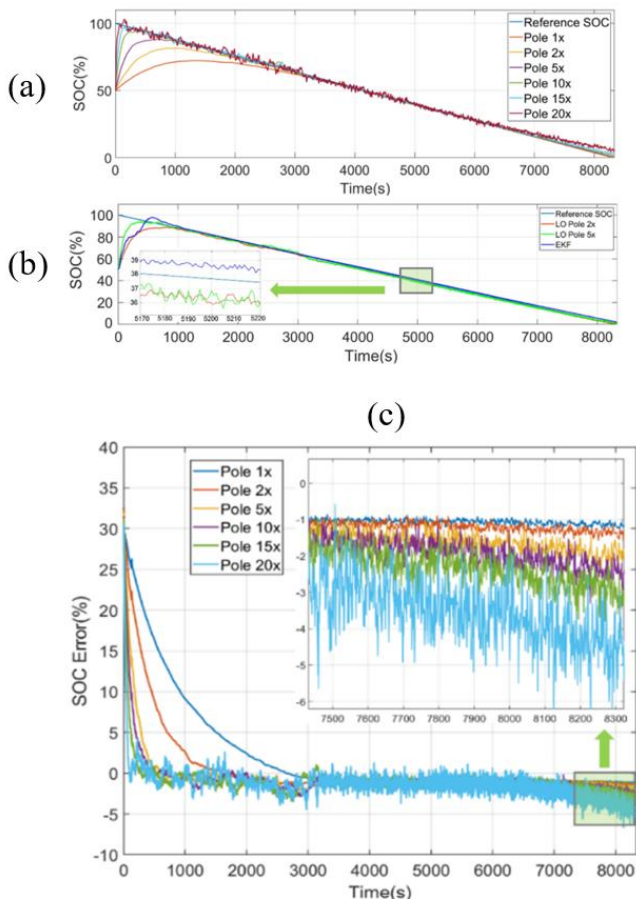
Fig. 11. SOC estimation error under different poles from 1-20 times faster than the slowest system poles (a) Compare with reference SOC, (b) Compare with EKF, (c) Closed-up view of SOC error in percent.

From Table 4, it can be observed that the total computational time was significantly increased when the model was changed from 1-RC to 2-RC, and from 2-RC to 3-RC. The average RMSE is found to be the lowest in the 3-RC model for both EFK and LO algorithms. But also takes the highest computational time. The change of computational time with respect to average RMSE shall be compared to determine the optimum level of the ECM model for SOC estimation, as shown in Fig. 12.
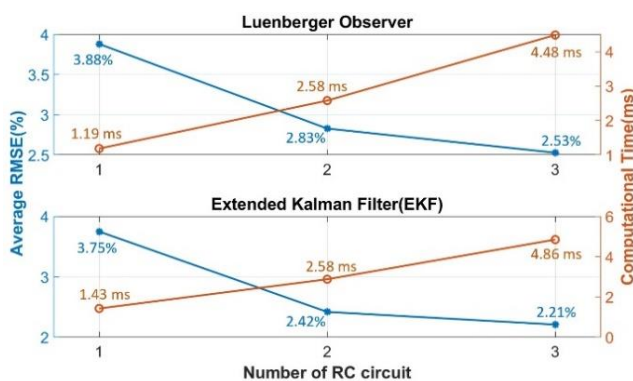

Fig. 12. Comparison of average RMSE and computational time under each level of ECM (upper) LO algorithm (lower) EKF algorithm.

From Fig. 12, changing the ECM from 1-RC to 2-RC has doubled the computational time in both LO and EKF algorithms, and the average RMSE decreased by 22.42% and 32.80% in LO and EKF, respectively. These decreases in RMSE are required to suppress the SOC estimation error lower than 3% in average. However, from 2-RC to 3-RC, the computation time increased by approximately 70% but the RMSE decreased only by 10.6% and 8.67% in LO and EKF, respectively. These decreases in RMSE are very small when being compared with the additional computational time required to run the 3-RC ECM, which is considered not worth it because the number of battery cells which the microcontroller can handle in one sampling time interval will be significantly lower than the case of using 2-RC ECM. Thus, it is recommended to use 2-RC ECM as an optimal trade-off between computational time and estimation accuracy.

4. Flexible BMS Design Example and Discussion

As mentioned in the introduction part that the flexibility of the previous works [2, 3, 9, 10] rarely mentioned the details of flexible hardware design because they focused primarily on certain purposes. Thus, another innovative topic of this study is to give a comprehensive design example of flexible BMS for automotive applications which utilized the knowledge presented previously. The goal of the flexible design shall achieve good scalability to support a wide range of number of cells and chemistries. The measurement parts shall have good accuracy and can be easily adapted with a little effort. The communication shall provide ease of data exchange between BMSs, or between other automotive systems, and shall be robust enough to tolerate interferences. This flexible design would help the BMS designers to reduce the development cycles when the design requirement is changed, resulting in less cost and time-to-market.
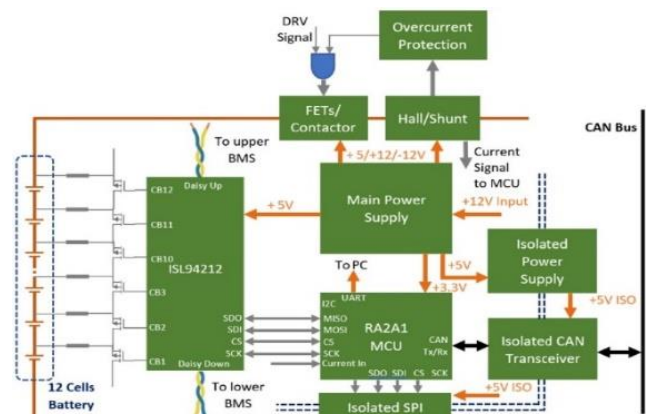

Fig. 13. Structure of the proposed flexible BMS.

Fig. 14. Actual board of the proposed flexible BMS (left) top layer (right) bottom layer.

PCB design and communication: the structure of the proposed flexible BMS is shown in Fig. 13 and its PCB was 130cm x 85cm as shown in Fig. 14, which is compact enough to be installed inside a small-size vehicle. The PCB mainly consists of 5 parts, BMS IC ISL94212, microcontroller RA2A1(MCU) with internal CAN controller, power supplies, isolated CAN driver and SPI, and passive balancing circuit. Each BMS board can supervise 6 to 12 cells, but can be stacked up to support up to 192 cells, making it suitable for hybrid/electric vehicles. In terms of scalability, the BMS board comes with an empty solder pad to install microcontroller, so the board can be used as a standalone centralized BMS (Fig. 15(a)) to supervise a small battery pack with 6-12 cells. However, to supervise a large-scale battery pack, the users can re-configure the board to be distributed BMS (Fig. 15(b)) by installing an MCU on the master board, then connecting all of the slave BMS modules to the master board via daisy chain as shown in Fig.16. The daisy chain in ISL94212 is a 2-wires communication that adopts an external RC circuit to terminate its differential port to increase the robustness against interference, and to provide a galvanic isolation up to 1000V. The data rate of daisy chain can be set up to 500 kHz. The maximum distance between each board is 2 meters, which is sufficient for automotive applications. In addition, the board is equipped with SPI and an isolated CAN driver, which can withstand up to 5kV. The data rate of CAN and SPI was set at 1Mbps, which is compliant with the ASIL-C standard. The CAN frame of RA2A1 MCU can support both 11 bits standard ID, and 29 bits CAN extended ID to support a large data transmission.
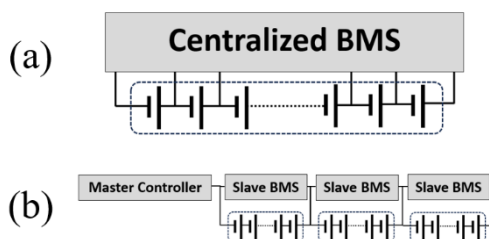

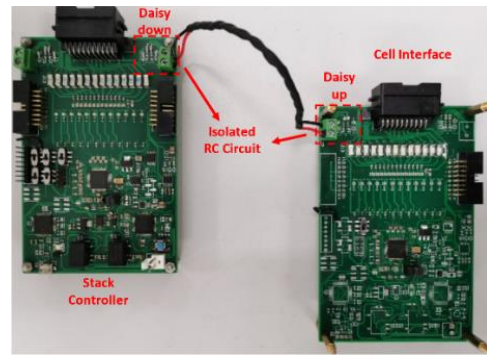Fig. 15. Structure of BMS (a) centralized BMS; (b) distributed BMS.

Fig. 16. Connection of two BMSs via Daisy chain communication.

Measurement: the ADCs of this BMS shown in Fig. 17, is 16-bit delta-sigma ADCs which can provide the measurement accuracy in the range of ±10mV, compliant with the ASIL-C requirements. The signal conditioning circuit as shown in Fig. 17 is designed to support both single-ended input or differential input. The single-ended input can reduce the space required for ground connection and lowering the cost. While the differential input provides more robustness against high inference. The solder pads R_Hall_1 and R_Hall_2 in Fig.17 are left available for installing shunt resistors, so the ADCs can support the connections of shunt current sensor, current-mode hall sensors (ex. LEM LA100p), and voltage-mode hall sensors (ex. LEM LXSR 6-NPS), and can be used in all noisy environment. In addition, to monitor the temperature using a thermistor, the ADCs were equipped with an LM334 current source, which converts the temperature-dependent of NTC/PTC to voltage. Users can easily change the configuration of ADCs by installing or removing the zero-ohm resistors shown in Fig. 17.
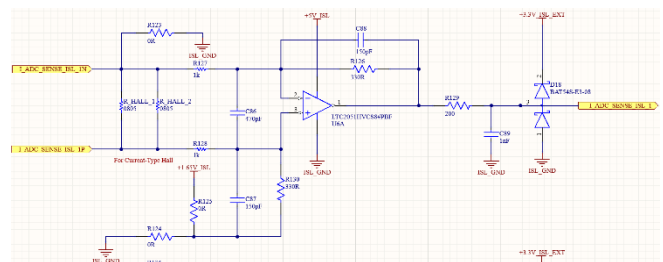

Fig. 17. Structure of flexible ADCs.

Power supply: the power supply of this BMS can generate 4 voltage levels, +3.3V, +5V, +12V, -12V, to supply all peripheral components including hall sensors and automotive contactors. In addition, +12V lead-acid battery can be used as the input of these power supply, so the board can be operated in standalone mode, even when the high-voltage battery pack is disconnected. **Protection:** the BMS is also equipped with 2 opto-isolated contactor drivers, to meet the safety requirements and ISO 26262. In the case of small vehicles, the contactor drivers can be used to operate the FETs to control the charge/discharge

process. **Balancing:** the proposed BMS uses passive balancing to equalize the SOC level of all cells. The value of balancing resistors ($R_{balancing}$) is determined based on the maximum balancing current recommended for 100 kWh EVs or PHEVs, which is 420mA as mentioned in the section 2.6. Assuming that the maximum unbalanced voltage is 2V, the value of $R_{balancing}$ can be approximated as $R_{balancing} \approx 2$ V /420 mA $\approx 4.76\Omega$, and the maximum power loss is around 0.83W. To handle this power loss, the solder pads with the size of 2512 SMD resistors are provided for installing the balancing resistors, which can dissipate up to 2W of power without the need for a heat sink, resulting in a smaller overall size.

The innovation of this study was made in terms of maximizing the level of scalability, adaptability, along with the compatibility with automotive standards. The flexible design is compact enough to be used in small automotive applications such as e-bikes but can be easily scaled up to supervise a medium-scale automotive battery pack, whose number of cells is less than 192 cells with the voltage level in the range of 36-1000 V, and the total power of less than 100 kWh. The built-in CAN bus supports both standard and extended ID with the baud rate of 1 Mbps, so it can be used to communicate directly with other systems such as vehicle control units (VCU), EV charger or a data logger. In term of software, the use of 2-RC ECM model provides the estimation accuracy in the range of 2.5%, and the computational time of around 2.6ms, which is fast enough to perform the SOC estimation of 192 cells under highly dynamic driving cycles such as UDDS or LA92.

Therefore, when the BMS requirement has been changed, such as changing the type of voltage or current sensor, or increasing/ decreasing the number of cells, the BMS designers can quickly re-adjust the system to suit the new requirement without having to spend a large effort to develop a new hardware or software, resulting in shorter development time and labour cost.

5. Real-time Testing: Passive Balancing

The real-time passive balancing in this study was performed using the SOC-based method. The balancing process starts from measuring the open-circuit-voltage (OCV) of all 24 cells, then determines the SOC level of all cells in a real-time using 2-ECM with EKF shown in the section 3. Then, sorting the values of SOC in descending order to search for the cell which has the lowest SOC. This lowest value will be used as a based-line value to determine the balancing time of each cell by using Eq. (23)

$$T_{balancing} \approx (SOC_{difference} \times R_{balancing}) / V_{cell} \quad (23)$$

where $R_{balancing}$ is set to be 25Ω to carry the balancing current around 150mA. The balancing process keeps going on until the SOC difference between the highest SOC cell and the lowest SOC cell is less than 3%. The terminal voltage was recorded by using Graphtec gl840 data logger, the real-time test setting is shown in Fig. 18.

Fig. 18. Real-time microcontroller-based experiment.

The sampling rate was set to be 1 second, corresponding to the sampling rate used in section 3. The battery cells under test are 24 cells Toriyama laptop series 2600mAh, with the actual capacity of 9360 C. The initial voltages of all cells before performing the balancing process are in the range of 3.77 to 3.86 V or SOC in the range of 49% to 57%, estimated from SOC-OCV curve shown in Fig. 5.
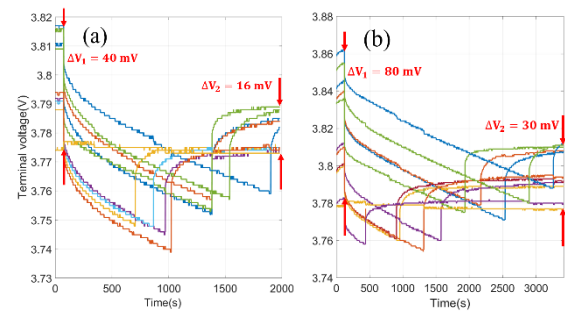

Fig. 19. Cell voltage during balancing (a) cells 1-12 (b) cells 13-24.

As shown in Fig. 19(a) and Fig. 19(b), the balancing process took around 2000 seconds to reduce the voltage difference from 40 mV ($\sim$3.75% ΔSOC) to 16 mV ($\sim$2% ΔSOC) and around 3500 seconds to reduce the voltage difference from 80 mV ($\sim$7.34% ΔSOC) to 30 mV ($\sim$2.88% ΔSOC). It can be seen that the balancing resolution of SOC-based method is very high that the unbalance of the cells can be reduced to less than 30mV ($\sim$2.88% ΔSOC). This resolution is comparable to the balancing criteria found in many studies [2, 12, 61, 62] that the BMS will terminate the balancing when the cells' voltage is in the range of 30-50mV ($\sim$2.88% - 5% ΔSOC).

6. Conclusion

In this study, a guideline on flexible battery management for automotive application has been presented by focusing on six crucial aspects, 1) voltage measurement 2) current measurement 3) Temperature acquisition 4) SOC estimation algorithm and 5) balancing

algorithm, by considering the real-life driving pattern, operation, size of battery and automotive standard. The results provide a quick suggestion on which configuration or balancing algorithm is suitable for a particular vehicle and particular battery pack. In the later section, a comparison of 3-levels ECM model under Luenberger observer and Extended Kalman Filter (EKF) has been performed to find out the optimal solution for a small-scale real-time BMS operation. The tests were performed under 3 standard driving conditions, UDDS, US06, LA92 and a pulse discharging of LiFePO$_4$ then, the estimation accuracy and the computational time of each test case were used as the criteria to evaluate the performance of each algorithm. The results suggest that the optimal ECM model for real-time SOC operation is the second order model which give the best trade-off between accuracy and computational burden. The pole of Luenberger observer should be set in the range of 2-5 times faster than the system poles to achieve a satisfying convergence performance while minimizing the disturbance on the system. These results can be used as a basic guideline to shorten development time when developing a BMS for automotive applications.

Acknowledgement

Reference

[1] T. A. Stuart and W. Zhu, "Modularized battery management for large lithium-ion cells," *Journal of Power Sources*, vol. 196, no. 1, pp. 462–464, 2011, doi:10.1016/j.jpowsour.2010.04.055.

[2] U. Abronzini, C. Attaianese, M. D. Monaco, F. Porpora, G. Tomasso, M. Granato, and G. Frattini, "Optimal modular BMS for high performances NMC battery pack," in *2018 IEEE International Conference on Electrical Systems for Aircraft, Railway, Ship Propulsion and Road Vehicles & International Transportation Electrification Conference (ESARS-ITEC)*, 2017, pp. 1–6.

[3] S. Jacobitz, S. Scherler, and X. Liu-Henke, "Model-based design of a scalable battery management system by using a low-cost Rapid Control Prototyping System," in *2018 Thirteenth International Conference on Ecological Vehicles and Renewable Energies (EVER)*, 2018, pp. 1–7, doi:10.1109/EVER.2018.8362402.

[4] J. Williams and M. Thoren, "Developments in battery stack voltage measurement," Linear Technology, Norwood, MA, Appl. Note, 112, 2007.

[5] A. Caliwag, K. L. Muh, S. H. Kang, J. Park, and W. Lim, "Design of modular battery management system with point-to-point SoC estimation algorithm, in *2020 International Conference on Artificial Intelligence in Information and Communication (ICAIIC)*, 2020, pp. 701–704.

[6] T. Stuart, F. Fang, X. Wang, C. Ashtiani, and A. Pesaran, "A modular battery management system for HEVs," *SAE Transactions*, vol. 111, pp. 777–785, 2002. [Online]. Available: http://www.jstor.org/stable/44699487

[7] I. Carlucho, R. de la Vega, M. Spina, and G. G. Acosta, "A modular battery management system for electric vehicles," in *2018 IEEE Biennial Congress of Argentina (ARGENCON)*, pp. 1–6.

[8] R. Di Rienzo, R. Roncella, R. Morello, F. Baronti, and R. Saletti, "Low-cost modular battery emulator for battery management system testing," in *2018 IEEE International Conference on Industrial Electronics for Sustainable Energy Systems (IESES)*, pp. 44–49, doi:10.1109/IESES.2018.8349848.

[9] H.-C. Chen, S.-S. Li, S.-L. Wu, and C.-Y. Lee, "Design of a modular battery management system for electric motorcycle, *Energies*, vol. 14, no. 12, 2021, doi:10.3390/en14123532.

[10] X. Zuo and C. Zhang, "Flexible design for battery management system," in *2016 International Conference on Network and Information Systems for Computers (ICNISC)*, IEEE, pp. 168–172.

[11] Maxim Integrated, "High-side current-sense measurement: Circuits and principles," Application Note, 2001.

[12] H. M. O. Canilang, A. C. Caliwag, and W. Lim, "Design, implementation, and deployment of modular battery management system for IoT-based applications," *IEEE Access*, vol. 10, pp. 109008-109028, 2022.

[13] K. Maniar, "Comparing shunt-and hall-based isolated current-sensing solutions in HEV/EV," Texas Instruments, SBAA293B, 2018.

[14] Texas Instruments, "Simplifying current sensing (Rev. A)," white paper slyy154, 2018.

[15] P. Weicker, *A Systems Approach to Lithium-Ion Battery Management*. Artech House, 2013.

[16] A. Zaitsev, D. Butarovich, and A. Smirnov, "Basic principles of automotive modular battery management system design," *IOP Conference Series: Materials Science and Engineering*, vol. 819, no. 1, p. 012024, 2020.

[17] S. Bob, "Improving Communications With the bq76PL536," Application Report No. SLUA562, 2010.

[18] Texas Instrument, "System trade-offs for high- and low-side current measurements," Analog - Technical Articles - TI E2E Support Forums, Jun. 2017. [Online]. Available: https://e2e.ti.com/blogs_/b/analogwire/posts/system-trade-offs-for-high-and-low-side-current-measurements

[19] Texas Instruments, "Load dump and cranking protection for automotive backlight LED power supply," Application Report SNVA681, 2013.

[20] Texas Instruments, "Using low-side FETs with the BQ769x2 battery monitor family," Application Report SLUAA84A, 2021.

[21] Texas Instrument, "Understanding current sensing in HEV/EV batteries," Automotive - Technical Articles - TI E2E Support Forums, Aug. 2017. [Online]. Available: https://e2e.ti.com/blogs_/b/behind_the_wheel/posts/understanding-current-sensing-in-hev-ev-batteries

[22] K. Maniar, "Comparing isolated amplifiers and isolated modulators," Texas Instrument, white paper SBAA359A, Feb. 2019.

[23] D. Marcos, M. Garmendia, J. Crego, and J. A. Cortajarena, "Functional safety BMS design methodology for automotive lithium-based batteries," *Energies*, vol. 14, no. 21, 2021, doi:10.3390/en14216942.

[24] Electronics Weekly. "Current sensing in an automotive environment." Electronics Weekly. [Online]. Available: https://www.electronicsweekly.com/news/current-sensing-automotive-environment-2019-02/

[25] Texas Instruments, "Automotive, mA-to-kA Range, Current Shunt Sensor Reference Design," TI Designs TIDA-03050, 2017.

[26] ROYPOW USA. "LiFePO4 Golf Cart Battery (Product Review)." [Online]. Available: http://www.roypowusa.com/?page_id=26237

[27] Porta Power. "Electric Bicycles Battery (Product Review)." [Online]. Available: https://portapower.com/

[28] Bourns, "Using current sense resistors for accurate current measurement," Application Note Bourns n1702, 2022.

[29] M. Grant, "Why use isolated amplifiers," in *User Manual DEWESoft*. 2021.

[30] G. Plett, *Battery Management Systems: Battery Modeling*. 2015, vol. I.

[31] Y. Fujita, Y. Hirose, Y. Kato, and T. Watanabe, "Development of battery management system," *Fujitsu Ten Tech. J*, vol. 42, no. 42, pp. 68-80, 2016.

[32] P. Leijen and N. Kularatna, "Developing a monitoring system for Toyota Prius battery-packs for longer term performance issues," in *Industrial Electronics (ISIE), 2013 IEEE International Symposium*, Washington, DC, USA, pp. 1-6.

[33] Y. Li, X. Wei, and Z. Sun, "Low power strategy design for battery management system, in *2009 International Conference on Measuring Technology and Mechatronics Automation*, vol. 2, pp. 636–639, doi:10.1109/ICMTMA.2009.415.

[34] J. Chatzakis, K. Kalaitzakis, N. C. Voulgaris, and S. N. Manias, "Designing a new generalized battery management system," *IEEE Transactions on Industrial Electronics*, vol. 50, no. 5, pp. 990–999, 2003, doi:10.1109/TIE.2003.817706.

[35] H. Roger and M. Willy, "BQ79606A-Q1 design recommendation," Texas Instruments, Application Report No. SLUA811C), 2019.

[36] G. Zimmer, "Highly accurate hybrid electric battery monitor," *Power Electronics Europe*, vol. 8, pp. 25-28, 2012.

[37] "Electric Vehicle Database." [Online]. Available: https://ev-database.org/

[38] Renesas, "Battery management system tutorial, white paper), 2018. [Online]. Available: https://www.renesas.com/us/en/document/whp/battery-management-system-tutorial

[39] M. Lelie, T. Braun, M. Knips, H. Nordmann, F. Ringbeck, H. Zappen, and D. U. Sauer, "Battery management system hardware concepts: An overview," *Applied Sciences*, vol. 8, no. 4, p. 534, 2018.

[40] H. Koepf, E. D. Wilkening, C. Klosinski, and M. Kurrat, "Breaking performance of protection devices for automotive dc powertrains with a voltage of 450 V," in *ICEC 2014 The 27th International Conference on Electrical Contacts*, Jun. 2014.

[41] L. H. J. Raijmakers, D. L. Danilov, R. A. Eichel, and P. H. L. Notten, "A review on various temperature-indication methods for Li-ion batteries," *Applied Energy*, vol. 240, pp. 918-945, 2019.

[42] Z. Wang, J. Ma, and L. Zhang, "Finite element thermal model and simulation for a cylindrical Li-ion battery," *IEEE Access*, vol. 5, pp. 15372-15379, 2017.

[43] Y. Lyu, A. R. M. Siddique, S. H. Majid, M. Biglarbegian, S. A. Gadsden, and S. Mahmud, "Electric vehicle battery thermal management system with thermoelectric cooling," *Energy Reports*, vol. 5, pp. 822-827, 2019.

[44] M. Swierczynski, D. I. Stroe, A. I. Stan, R. Teodorescu, and S. K. Kær, "Investigation on the self-discharge of the LiFePO 4/C nanophosphate battery chemistry at different conditions, in *2014 IEEE Conference and Expo Transportation Electrification Asia-Pacific (ITEC Asia-Pacific)*, IEEE, Aug. 2017, pp. 1-6.

[45] S. Arora and A. Kapoor, "Experimental study of heat generation rate during discharge of lifePO4 pouch cells of different nominal capacities and thickness," *Batteries*, vol. 5, no. 4, p. 70, 2019.

[46] Q. Zhang, D. Wang, B. Yang, X. Cui, and X. Li, "Electrochemical model of lithium-ion battery for wide frequency range applications," *Electrochimica Acta*, vol. 343, p. 136094, 2020.

[47] Z. A. Khan, P. Shrivastava, S. M. Amrr, S. Mekhilef, A. A. Algethami, M. Seyedmahmoudian, and A. Stojcevski, "A comparative study on different online state of charge estimation algorithms for lithium-ion batteries," *Sustainability*, vol. 14, no. 12, p. 7412, 2022.

[48] B. Xia, W. Zheng, R. Zhang, Z. Lao, and Z. Sun, "A novel observer for lithium-ion battery state of charge estimation in electric vehicles based on a second-

order equivalent circuit model," *Energies*, vol. 10, no. 8, p. 1150, 2017.

[49] J. Meng, M. Boukhnifer, and D. Diallo, "Comparative study of lithium‑ion battery open‑circuit‑voltage online estimation methods," *IET Electrical Systems in Transportation*, vol. 10, no. 2, pp. 162-169, 2020.

[50] United States Department of Energy, Idaho National Laboratory, *PNGV Battery Test Manual, DOE/ID-10597, Revision 3*. 2001.

[51] N. Chen, P. Zhang, J. Dai, and W. Gui, "Estimating the state-of-charge of lithium-ion battery using an H-infinity observer based on electrochemical impedance model," *IEEE Access*, vol. 8, pp. 26872-26884, 2020.

[52] K. Ogata, *Modern Control Engineering*. Upper Saddle River, NJ: Prentice Hall, 2010, vol. 5.

[53] P. Kollmeyer, C. Vidal, M. Naguib, and M. Skells, 2020, "Lg 18650HG2 li-ion battery data and example deep neural network xEV SOC estimator script, Mendeley Data, 3."

[54] A. Narayan, "State and parametric estimation of li-ion batteries in electrified vehicles," M.S. thesis, School of Electrical Engineering, KTH Royal Institute of Technology, Sweden, 2017.

[55] S. Moura, "State Estimation. CE 295 — Energy Systems and Control," University of California, Berkeley, 2018, ch. 2. [Online]. Available: https://ecal.berkeley.edu/files/ce295/CH02-StateEstimation.pdf

[56] J. K. Barillas, J. Li, C. Günther, and M. A. Danzer, "A comparative study and validation of state estimation algorithms for Li-ion batteries in battery management systems," *Applied Energy*, vol. 155, pp. 455-462, 2015.

[57] D. Andrea, *Battery Management Systems for Large Lithium-Ion Battery Packs*. Artech House, 2010.

[58] M. Hammouche, A. Mohand-Ousaid, P. Lutz, and M. Rakotondrabe, "Robust interval Luenberger observer-based state feedback control: Application to a multi-DoF micropositioner," *IEEE Transactions on Control Systems Technology*, vol. 27, no. 6, pp. 2672-2679, 2018.

[59] Renesas Electronics. "Sensing Elements for Current Measurements." [Online]. Available: https://www.renesas.com/us/en/document/whp/sensing-elements-current-measurements

[60] M. Kultgen, "Managing high-voltage lithium-ion batteries in HEVs. EDN," Electrical Design News, vol. 54, no. 7, p. 45, 2009.

[61] S. Kıvrak, T. Özer, Y. Oğuz, and E. B. Erken, "Battery management system implementation with the passive control method using MOSFET as a load," *Measurement and Control*, vol. 53, no. 1-2, pp. 205-213, 2020, doi:10.1177/0020294019883401.

[62] S. Kivrak, T. Özer and Y. Oğuz, "Battery management system implementation with passive control method," in *IV International Conference on Information Technologies in Engineering Education (Inforino)*, Moscow, Russia, 2018, pp. 1-4, doi: 10.1109/INFORINO.2018.8581758.

[63] S. Kıvrak, T. Özer, Y. Oğuz, et al., "Novel active and passive balancing method-based battery management system design and implementation," J. Power Electron, vol. 21, pp. 1855–1865, 2021. [Online]. Available: https://doi.org/10.1007/s43236-021-00320-x

[64] S. Kıvrak, "Can bus based BMS control card design and implementation by using Stm32f103 series microcontroller," in *5th International Conference on Engineering Sciences*, Ankara, Turkey, 2019, pp. 1-8.

[65] Y. F. Kurt and T. Özer, "13S battery pack and battery management system design and implementation for electric bicycles, *International Journal of Automotive Science and Technology*, vol. 7, no. 2, pp. 87-94, 2023, doi:10.30939/ijastech.1246624.

Napat Trongnukul, photograph and biography not available at the time of publication.

Nisai H. Fuengwarodsakul, photograph and biography not available at the time of publication.

Manop Masomtob, photograph and biography not available at the time of publication.